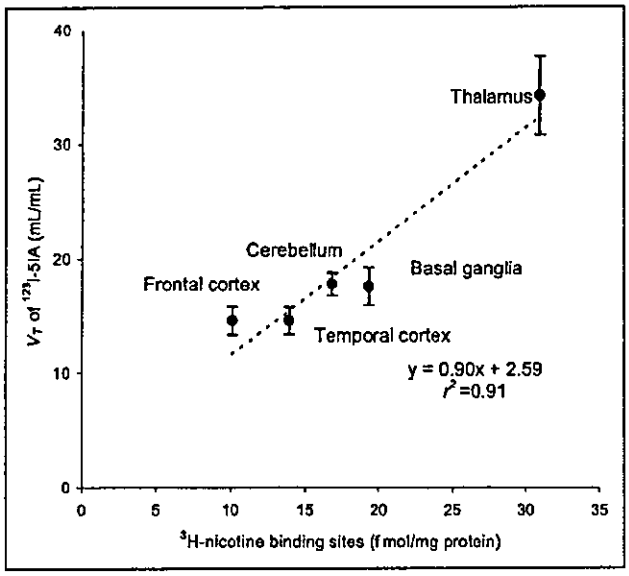

FIGURE 6. Correlation between distribution volumes described for ^{123}I-5IA at 360 min after injection with those specific bindings for (−)-^{3}H-nicotine in postmortem study (r^2 = 0.91) (*10*).

Furthermore, although the density of the $\alpha_4\beta_2$ subtype of nAChR in the cerebellum was lower in animals, a substantial presence was found in the human brain (*2*). Therefore, the cerebellum is an inappropriate reference region in quantitative studies using ^{123}I-5IA in humans. The study also indicated that there is no other receptor-poor region that is appropriate as a reference region for SPECT (*2*). Thus, use of the reference region is not applicable to the quantification of nAChR in the human brain.

In the present study, the rate parameter constant K_1' showed relative low values (0.25 ± 0.04 in cerebellum at 90-min scan time, Table 4). The K_1' represents the delivery rate constant from the plasma to the tissue compartment (C_{f+ns+s}), and it is basically driven by the regional cerebral blood flow (F) and the single-pass extraction fraction of the ligand into the brain (E_0). Considering that the cerebral blood flow is normal in the groups of subjects, the extraction fraction of ^{123}I-5IA might be the reason for these lower values. Saji et al. (*18*) showed in an animal study that ^{123}I-5IA has a moderate brain uptake index (BUI = 31 ± 6), which was lower than that of nicotine (BUI = 103 ± 12). These findings are in complete agreement with our results.

Besides the simplicity of the method and the independency of the model configuration of the tissue compartment, the application of graphical analysis for determination of distribution volumes (V_{LG}) in receptor binding studies offers greater accuracy. The main outcome from this method of measurement can be estimated with much higher accuracy than individual parameters of radioligand kinetics (*32*). In the present study, the highest slopes correlated with those regions with higher densities of nAChRs in the human brain using ^{123}I-5IA SPECT (*2*). The analysis of the correlation between V_T and V_{LG} values showed good agreement (r^2 = 0.99) (Fig. 7) as well as between the transfer constant K_1' and K^*_1 (r^2 = 0.96) ($P < 0.01$, for both). The results indicate that the graphical method showed essentially the same information of measurement of nAChRs using ^{123}I-5IA SPECT with acceptable accuracy.

Taking account of all factors that determine the V_T values of ^{123}I-5IA in the present study, 2 independent variables were identified: regions in the brain and length of data acquisition. The variable subject was not considered due to the uniform population evaluated in this study (age of subjects around 20 y in group 1 subjects). The variability of receptor densities and metabolism of ^{123}I-5IA should be quite small in such a uniform population, and distribution volumes would be successfully estimated from data of a short scan time because biases caused by short data should be similar in all subjects. Thus, a factorial ANOVA was applied considering all factors together. The results showed that the length of the scan was not critical to determining the distribution volume in different brain regions. The factor region in the brain was significant and this finding can be easily explained by the differences in the V_T values between those regions in the brain. Once both factors interacted as a single term (region length), the results showed no statistical significance, so the region and length effects can be assumed to be consistent across levels of the other factor. Therefore, a short scan time (i.e., 90-min) can be used to evaluate the distribution volume in human brain using ^{123}I-5IA.

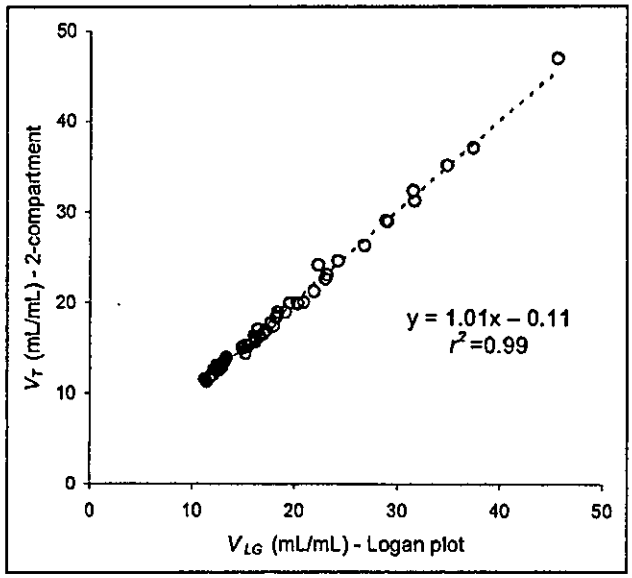

FIGURE 7. Analysis of correlation between distribution volumes from compartmental model (V_T) and graphical analyses (V_{LG}) performed during 360-min scan time. Circles represent V_T and V_{LG} values in various brain regions analyzed from all subjects in first group of volunteers. V_T and V_{LG} values from 2-compartment model and Logan plot analyses demonstrated high correlation index (r^2 = 0.99) ($P < 0.01$).

However, the factorial ANOVA has shown that the scan length was not of critical importance in determining the V_T values in the human brain regions; the 6-h scan time seems to have allowed more sensitive evaluation of the thalamic region. That is because the kinetics of ^{123}I-5IA in the human brain have some peculiarities for the thalamus (later peak of radioactivity in the brain around 110 min), making the longer scans more suitable for estimating the nAChRs in the thalamic regions.

Based on these results, another group of subjects (group 2) was included and scanned using a short scan time (90 min) (Table 4). To verify the reproducibility of measurement using a short scan time, subjects of around 20 y old were grouped (subjects 7–13). The V_T values were calculated and their results were compared with those V_T values calculated from the first group (using a 90-min time interval) for the same age (subjects 1–6). No significant difference was observed between them, confirming the reproducibility of the measurement with a short scan time.

Once the data for all volunteers (first group analyzed in a 90-min time interval and second group) were assembled in a single group (Table 4), the distribution of V_T values showed a pattern similar to that described for the 6-h scan time, with the highest V_T values for the thalamus (ANOVA, $P < 0.01$). Some studies have mentioned aged-related changes in the nicotinic neuroreceptors in the human brain (*2,7,10*), but our study did not observe statistically significant values. The inability to observe age-related changes in this study is probably due to the small number of subjects from different age groups. Further studies might be necessary to elucidate the age-related change in human nAChRs.

CONCLUSION

We have described a novel method for the quantitative analysis of nAChRs in the human brain using ^{123}I-5IA. A 2-compartment model analysis (2-parameter configuration) was chosen to fit the present data, and results were relatively stable across all regions. Three different levels of density of nAChRs in the human brain (expressed as V_T) were identified. The V_T values showed the highest density of nAChRs to be in the thalamus; moderate densities were found in the brain stem, basal ganglia, and cerebellum, and low densities were found in the frontal, parietal, temporal, and occipital cortices. Good agreement was observed between V_T values and autoradiographic studies done in vitro for nAChR density in human brain. A high correlation index was observed between distribution volumes from the compartmental model and graphical analyses. Our results indicate that ^{123}I-5IA SPECT is suitable for the quantification of nAChRs in the human brain.

ACKNOWLEDGMENTS

The authors thank Dr. Sadahiko Nishizawa, Hamamatsu Medical Photonics Foundation, for valuable comments, and Dr. Mahbubur Rahman, Department of Epidemiological and Clinical Research Information Management, Kyoto University, for advice regarding the statistical analysis. This work was supported in part by a grant from the Research for the Future Program of the Japan Society for the Promotion of Science (JSPS-RFTF97K00201), Grants-in-Aid for Scientific Research from the Ministry of Education, Science and Technology of Japan, a research grant for Longevity Sciences from the Ministry of Health and Welfare, and a grant from the Smoking Reseach Foundation. The authors thank Nihon Medi-Physics Co. Ltd., Japan, for providing sodium ^{123}I-iodide.

REFERENCES

1. Lindstrom J, Anand R, Peng X, Gerzanich V, Wang F, Li Y. Neuronal nicotinic receptor subtypes. *Ann NY Acad Sci.* 1995;757:100–116.
2. Paterson D, Nordberg A. Neuronal nicotinic receptors in the human brain. *Prog Neurobiol.* 2000;61:75–111.
3. Whiting P, Esch F, Shimasaki S, Lindstrom J. Neuronal nicotinic acetylcholine receptor beta-subunit is coded for by the cDNA clone alpha 4. *FEBS Lett.* 1987;219:459–463.
4. Flores CM, Rogers SW, Pabreza LA, Wolfe BB, Kellar KJ. A subtype of nicotinic cholinergic receptor in rat brain is composed of alpha 4 and beta 2 subunits and is up-regulated by chronic nicotine treatment. *Mol Pharmacol.* 1992;41:31–37.
5. Zoli M, Lena C, Picciotto MR, Changeux JP. Identification of four classes of brain nicotinic receptors using beta2 mutant mice. *J Neurosci.* 1998;18:4461–4472.
6. Changeux JP, Bertrand D, Corringer PJ, et al. Brain nicotinic receptors: structure and regulation, role in learning and reinforcement. *Brain Res Brain Res Rev.* 1998;26:198–216.
7. Whitehouse PJ, Au KS. Cholinergic receptors in aging and Alzheimer's disease. *Prog Neuropsychopharmacol Biol Psychiatry.* 1986;10:665–676.
8. Perry EK, Morris CM, Court JA, et al. Alteration in nicotine binding sites in Parkinson's disease, Lewy body dementia and Alzheimer's disease: possible index of early neuropathology. *Neuroscience.* 1995;64:385–395.
9. Silver W, Gillberg PG, Svensson AL, Nordberg A. Autoradiographic comparison of [^{3}H]-nicotine, [^{3}H]cytisine and [^{3}H]epibatidine binding in relation to vesicular acetylcholine transport sites in the temporal cortex in Alzheimer's disease. *Neuroscience.* 1999;94:685–696.
10. Shimohama S, Taniguchi T, Fujiwara M, Kameyama M. Changes in nicotinic and muscarinic cholinergic receptors in Alzheimer-type dementia. *J Neurochem.* 1986;46:288–293.
11. Marks MJ, Romm E, Gaffney DK, Collins AC. Nicotine-induced tolerance and receptor changes in four mouse strains. *J Pharmacol Exp Ther.* 1986;237:809–819.
12. Benwell ME, Balfour DJ, Anderson JM. Evidence that tobacco smoking increases the density of (–)-[^{3}H]nicotine binding sites in human brain. *J Neurochem.* 1988;50:1243–1247.
13. Perry DC, Davila-Garcia MI, Stockmeier CA, Kellar KJ. Increased nicotinic receptors in brains from smokers: membrane binding and autoradiography studies. *J Pharmacol Exp Ther.* 1999;289:1545–1552.
14. Breese CR, Marks MJ, Logel J, et al. Effect of smoking history on [^{3}H]nicotine binding in human postmortem brain. *J Pharmacol Exp Ther.* 1997;282:7–13.
15. Sullivan JP, Donnelly-Roberts D, Briggs CA, et al. A-85380 [3-(2(S)-azetidinylmethoxy)pyridine]: in vitro pharmacological properties of a novel, high affinity alpha 4 beta 2 nicotinic acetylcholine receptor ligand. *Neuropharmacology.* 1996;35:725–734.
16. Koren AO, Horti AG, Mukhin AG, et al. 2-, 5-, and 6-Halo-3-(2(S)-azetidinylmethoxy)pyridines: synthesis, affinity for nicotinic acetylcholine receptors, and molecular modeling. *J Med Chem.* 1998;41:3690–3698.
17. Mukhin AG, Gundisch D, Horti AG, et al. 5-Iodo-A-85380, an alpha4beta2 subtype-selective ligand for nicotinic acetylcholine receptors. *Mol Pharmacol.* 2000;57:642–649.
18. Saji H, Ogawa M, Ueda M, et al. Evaluation of radioiodinated 5-iodo-3-(2(S)-azetidinylmethoxy)pyridine as a ligand for SPECT investigations of brain nicotinic acetylcholine receptors. *Ann Nucl Med.* 2002;16:189–200.
19. Chefer SI, Horti AG, Lee KS, et al. In vivo imaging of brain nicotinic acetylcholine receptors with 5-[^{123}I]iodo-A-85380 using single photon emission computed tomography. *Life Sci.* 1998;63:PL355–PL360.

20 Musachio JL, Scheffel U, Finley PA, et al. 5-[I-125/123]iodo-3(2(S)-azetidinylmethoxy)pyridine, a radioiodinated analog of A-85380 for in vivo studies of central nicotinic acetylcholine receptors. *Life Sci.* 1998;62:PL351–PL357.
21 Musachio JL, Villemagne VL, Scheffel UA, et al. Synthesis of an I-123 analog of A-85380 and preliminary SPECT imaging of nicotinic receptors in baboon. *Nucl Med Biol.* 1999;26:201–207.
22 Fujita M, Tamagnan G, Zoghbi SS, et al. Measurement of $\alpha_4\beta_2$ nicotinic acetylcholine receptors with [^{123}I]5-I-A-85380 SPECT. *J Nucl Med.* 2000;41:1552–1560.
23 Fujita M, Seibyl JP, Vaupel B, et al. Whole-body biodistribution, radiation absorbed dose, and brain SPET imaging with [^{123}I]5-I-A-85380 in healthy human subjects. *Eur J Nucl Med.* 2002;29:183–190.
24 Vaupel DB, Tella SR, Huso DL, et al. Pharmacology, toxicology, and radiation dosimetry evaluation of [I-123]5-I-a-85380, a radioligand for in vivo imaging of cerebral neuronal nicotinic acetylcholine receptors in humans. *Drug Dev Res.* 2003;58:149–168.
25 Mintun MA, Raichle ME, Kilbourn MR, Wooten GF, Welch MJ. A quantitative model for the in vivo assessment of drug binding sites with positron emission tomography. *Ann Neurol.* 1984;15:217–227.
26 Logan J, Fowler JS, Volkow ND, et al. Graphical analysis of reversible radioligand binding from time-activity measurements applied to [N-^{11}C-methyl]-(-)-cocaine PET studies in human subjects. *J Cereb Blood Flow Metab.* 1990;10:740–747.
27 Ding Y, Liu N, Wang T, et al. Synthesis and evaluation of 6-[^{18}F]fluoro-3-(2(S)-azetidinylmethoxy)pyridine as a PET tracer for nicotinic acetylcholine receptors. *Nucl Med Biol.* 2000;27:381–389.
28 Kimes AS, Horti AG, London ED, et al. 2-[^{18}F]F-A-85380: PET imaging of brain nicotinic acetylcholine receptors and whole body distribution in humans. *FASEB J.* 2003;17:1331–1333.
29 Marutle A, Warpman U, Bogdanovic N, Nordberg A. Regional distribution of subtypes of nicotinic receptors in human brain and effect of aging studied by (±)-[^{3}H]epibatidine. *Brain Res.* 1998;801:143–149.
30 Xiao Y, Meyer EL, Thompson JM, Surin A, Wroblewski J, Kellar KJ. Rat alpha3/beta4 subtype of neuronal nicotinic acetylcholine receptor stably expressed in a transfected cell line: pharmacology of ligand binding and function. *Mol Pharmacol.* 1998;54:322–333.
31 Kulak JM, Sum J, Musachio JL, McIntosh JM, Quik M. 5-Iodo-A-85380 binds to α-conotoxin MII-sensitive nicotinic acetylcholine receptors (nAChRs) as well as α4β2* subtypes. *J Neurochem.* 2002;81:403–406.
32 Carson RE. Mathematical modeling and compartmental analysis. In: Harbert J, Eckelman WC, Neumann R, eds. *Nuclear Medicine: Diagnosis and Therapy.* New York, NY: Thieme Medical; 1996:167–194.

Annals of Nuclear Medicine Vol. 18, No. 4, 337–344, 2004

5-[^{123}I]Iodo-A-85380: assessment of pharmacological safety, radiation dosimetry and SPECT imaging of brain nicotinic receptors in healthy human subjects

Masashi UEDA,* Yasuhiko IIDA,* Takahiro MUKAI,** Marcelo MAMEDE,** Koichi ISHIZU,** Mikako OGAWA,*** Yasuhiro MAGATA,*** Junji KONISHI** and Hideo SAJI*

*Department of Patho-Functional Bioanalysis, Graduate School of Pharmaceutical Sciences, Kyoto University
**Department of Nuclear Medicine and Diagnostic Imaging, Graduate School of Medicine, Kyoto University
***Laboratory of Genome-Bio Photonics, Photon Medical Research Center, Hamamatsu University School of Medicine

Recently, 5-[^{123}I]iodo-3-(2(*S*)-azetidinylmethoxy)pyridine ([^{123}I]5IA) was developed as a ligand for imaging the nicotinic acetylcholine receptor (nAChR) in human brain using single photon emission computed tomography (SPECT). In the present study, the toxicity and radiation absorbed dose of [^{123}I]5IA were investigated.

Behavior and physiological parameters were examined in mice and rats after administration of 5IA. There were no changes in these parameters in animals administered 1 μg/kg of 5IA or less, indicating that the no observed effect level (NOEL) of 5IA was 1 μg/kg. [^{123}I]5IA was then administered to healthy human subjects and serial whole-body images were acquired over 24 hr. Initially, high levels of radioactivity were observed in the liver and urinary bladder and moderate levels in the lungs, kidneys, and brain. Whole brain activity at 1 hr was 4.6 ± 0.4% of the injected dose and this value gradually decreased with time. The majority (~75%) of the radioactivity was excreted in urine within 24 hr, and less than 1% remained in all organs tested. The biological half-life of [^{123}I]5IA averaged 7.2 ± 4.0 hr. Based on the biodistribution data, radiation absorbed doses were estimated using MIRDOSE 3.1 software with the dynamic bladder model and the ICRP gastrointestinal (GI) tract model. Consequently, the effective dose equivalent was estimated to be 30 ± 1.4 μSv/MBq, which is an acceptable radiation burden. Having determined the safety of this compound, we performed SPECT imaging in a healthy human subject using 171 MBq of [^{123}I]5IA. SPECT images clearly revealed a cerebral distribution of radioactivity that was consistent with the known distribution of central nAChRs in humans. These results suggest that [^{123}I]5IA is a promising ligand for imaging nAChRs in humans, with an acceptable dosimetry and pharmacological safety at the dose required for adequate SPECT imaging.

Key words: 5-[^{123}I]iodo-3-(2(*S*)-azetidinylmethoxy)pyridine, pharmacological effects, radiation dosimetry, single photon emission computed tomography, nicotinic acetylcholine receptor

INTRODUCTION

NICOTINIC ACETYLCHOLINE RECEPTORS (nAChRs) are a family of ligand-gated ion channels that regulate neurotransmission in the central and peripheral nervous systems. These receptors are of great interest because they are implicated in various brain functions, such as cognition and memory,[1,2] and in nicotine-induced neuroprotective[3] and analgesic effects.[4] In addition, changes in the density of nAChRs have been reported in various neurodegenerative disorders including Alzheimer's disease[5,6] and Parkinson's disease.[7,8] Thus, imaging of nAChRs in the brain with positron emission tomography (PET) or single photon emission computed tomography (SPECT) has been of

Received December 13, 2003, revision accepted March 11, 2004.

For reprint contact: Hideo Saji, M.D., Department of Patho-Functional Bioanalysis, Graduate School of Pharmaceutical Sciences, Kyoto University, Yoshida Shimoadachi-cho, Sakyo-ku, Kyoto 606-8501, JAPAN.
E-mail: hsaji@pharm.kyoto-u.ac.jp

great interest for the evaluation of brain functions and the diagnosis of neurodegenerative disorders. The development of a radioligand suitable for this purpose has been desired.

Recently, 5-[^{123}I]iodo-3-(2(*S*)-azetidinylmethoxy) pyridine (5IA), a derivative of A-85380 iodinated at the 5-position of the pyridine ring, was reported to be a promising ligand for imaging nAChRs because of its high uptake in the rodent and primate brain, a distribution consistent with the known density of nAChRs, and low non-specific binding.[9–13] Thus, characterization of its pharmacological effects and information on its biodistribution and organ radiation burden in humans have been required for the clinical application of [^{123}I]5IA brain SPECT.

The Food and Drug Administration proposes that a test compound be administered to small numbers of animals to identify doses causing no adverse effect and does not recommend calculating lethality parameters using large numbers of animals.[14] In the present study, we investigated changes in behavior in mice and in physiological parameters in rats after administration of 5IA to determine the NOEL of this ligand. Based on these results, the dose of [^{123}I]5IA was determined and then administered to healthy human volunteers to measure the whole-body distribution, to estimate the radiation absorbed doses, and to obtain SPECT images of [^{123}I]5IA in the human brain.

MATERIALS AND METHODS

Chemicals

5IA and 5-(tri-*n*-butylstannyl)-3-(1-*tert*-butoxycarbonyl-2(*S*)-azetidinylmethoxy)pyridine, the stannyl precursor of [^{123}I]5IA, were synthesized according to a previous report.[13] No carrier-added sodium [^{123}I]iodine was supplied by Nihon Medi-Physics Co. Ltd. (Nishinomiya, Japan). All other chemicals used were of reagent grade.

Studies in animals

Male ICR mice and male Sprague-Dawley rats were supplied by Japan SLC Co. Ltd. (Hamamatsu, Japan). The animal experiments were conducted in accordance with our institutional guidelines and approved by the Kyoto University Animal Care Committee. 5IA was injected as a physiological saline solution.

Behavioral test

Male ICR mice weighing 28–32 g were separated into four groups (five per group) and injected intravenously with either vehicle or one of three doses of 5IA: 10 μg/kg = 27.5 nmol/kg, 1 μg/kg = 2.75 nmol/kg, or 0.1 μg/kg = 0.275 nmol/kg. For 60 min after the administration, the righting reflex, motor functions and spontaneous locomotion were observed. Mice were bred for another week after 5IA administration, and the sub-acute toxicity of 5IA was assessed by measuring their weights.

Changes in physiological parameters

Male Sprague-Dawley rats weighing 280–320 g were anesthetized with chloral hydrate (400 mg/kg intraperitoneal injection) and implanted with a catheter into the left femoral artery. The catheter was connected through a three-way stopcock to a pressure transducer (COBE, Cobe Laboratory Inc., USA) and a monitor (CM-861, Fukuda Denshi Co. Ltd., Tokyo, Japan) for measuring arterial blood pressure. Heart rate, respiratory rate, blood gases (PCO_2 and PO_2), and blood pH were also measured. Heart rate was measured using the same monitor. Respiratory rate was counted with the naked eye. Blood pH and blood gases were determined with a dedicated analyzer (M278 Blood Gas System, Ciba-Corning, Germany). Prior to the administration of 5IA, basal values of each parameter were obtained.

Rats were separated into four groups (four or five per group) and injected intravenously with vehicle or one of three doses of 5IA: 5 μg/kg = 13.8 nmol/kg, 2 μg/kg = 5.51 nmol/kg, or 1 μg/kg = 2.75 nmol/kg. Mean arterial blood pressure (MABP) and heart rate were monitored continuously up to 60 min after the administration of each drug. The respiratory rate was counted 1, 2, 3, 5, 15, 30, 45, and 60 min after the administration. Blood pH and blood gases were determined by withdrawing blood via the three-way stopcock at 5, 15, 30, 45, and 60 min. The body temperature of each rat was maintained at 37°C throughout the study.

Data were analyzed using a one-way analysis of variance (ANOVA) followed by Dunnett's test to compare the parameters after the drug administration to the baseline. Differences were considered significant when $p < 0.05$.

Studies in humans

These experiments were approved by the Institutional Review Board of Kyoto University Hospital.

Radiolabeling

Radiolabeling was performed according to a previous report[13] with slight modifications. Briefly, reagents were added into a vial in the following order: no-carrier-added sodium [^{123}I]iodine (1110 MBq), 100 μg of stannyl precursor (10 μl of ethanolic solution), 160 μl of 1.5% acetic acid, 10 μl of 3 mol/l HCl, and 20 μl of 5% H_2O_2 solution as an oxidant. The mixture was stirred at 75°C for 15 min. Concentrated HCl was then added and the resulting solution stirred for 10 min at 75°C. The mixture was basified with sodium hydroxide, extracted with ethyl acetate, and purified by reverse-phase HPLC. After rotary evaporation of the eluent, the residue was formulated in 0.9% saline and filtered through a 0.2 μm filter into a sterile vial. Sterility was confirmed by lack of growth in tryptone soya broth/gelatin peptone. No endotoxin was detected by a limulus test based on the ability of endotoxin to induce coagulation of the amebocyte lysate of the horseshoe crab, *Limulus polyphemus*. Radiochemical yield was more

than 40% and radiochemical purity was greater than 98%. The specific activity determined from the UV absorbance at 254 nm was more than 169 GBq/μmol (the limit of detection with this method).

Subjects

Three healthy males were recruited for the whole-body scan (age: 19, 20, 67 years) and another healthy male was recruited for the brain SPECT (age: 20 years). All volunteers were nonsmokers. Before the imaging, written informed consent was obtained from each participant.

Whole-body image acquisition

Volunteers were positioned supine with their arms alongside their body. Whole-body images were acquired using a dual-headed gamma camera (RC-2500IV, Hitachi Medical Co., Tokyo, Japan). In this system, a low-energy high-resolution collimator was used, and the energy peak was centered at 159 keV with a 20% energy window.

Whole-body planar images were acquired 0.5, 1, 2, 5 and 24 hr after the injection of 100 MBq of [^{123}I]5IA. Acquisition was performed simultaneously in anterior and posterior positions. The scan speed was 15 cm/min and Matrix size was 256 × 1024 pixels.

Urine collection

Urine was collected up to 24 hr after injection. The volunteers were briefed to collect their urine and to record the volume and time of voidance. From each urine sample, three aliquots were measured in an automatic gamma counter (Aloka Co. Ltd., Tokyo, Japan). Measurements of radioactivity were corrected for physical decay and multiplied by the urine volume at each voidance. The total amount of radioactivity was expressed as a percentage of the injected radioactivity (% ID) of [^{123}I]5IA.

Image analysis

The quantification of uptake after injection of [^{123}I]5IA was performed using a region of interest (ROI) method. ROIs were drawn over the whole-body or various organs (brain, thyroid, lungs, heart, liver, spleen, abdomen, and left kidney) using HARP-III (Hitachi Medical Co., Tokyo, Japan). All ROIs were drawn by the same operator to minimize variability in region definition. The activity in the abdomen meant the gastrointestinal activity excluding liver, spleen, kidneys, and urinary bladder. The activity in kidneys was determined by doubling that in the left kidney, i.e., the activity in the right kidney was taken to be the same as that in the left. This was done to avoid overestimating the activity in the right kidney due to overlap with the liver. Almost all ROIs (except for the thyroid, which was drawn on the latest image) were drawn on the earliest images, and the shapes and sizes were kept constant in all subsequent images. ROIs drawn on the off-body region beside the volunteer's head were used as the instrumental background. After subtracting the instrumental background activity from the organ activity (as counts/pixel), the geometric mean of the anterior and posterior counts for the whole-body or each organ was calculated. The whole-body geometric mean count of the first scan was taken as the injected radioactivity, because the first images were acquired before excretion. The activity of the whole-body or each organ was calculated with the following equation: (geometric mean counts in whole-body or organ at each time point)/(geometric mean counts in first whole-body) × 100, and expressed as % ID.

Estimating radiation absorbed dose

For each individual, non-decay-corrected time-activity curves were generated for the brain, thyroid, lungs, heart, liver, spleen, and kidney. The terminal elimination phase

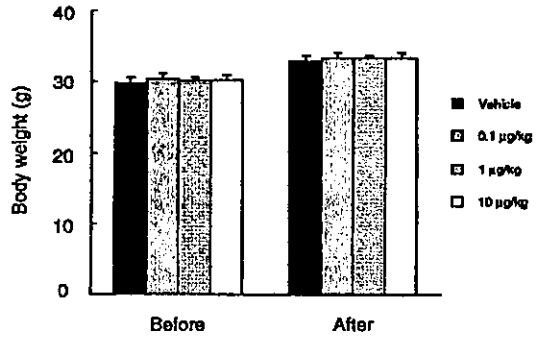

Fig. 1 Changes in body weight after administration of 5IA or vehicle. Mice were weighed before (Before) and 7 days after administration (After). No significant difference was observed between vehicle and 5IA-treated groups at either time point.

Table 1 Changes in behaviors after administration of 5IA

	Righting reflex		Grooming		Spontaneous locomotion	
	0–30 min	30–60 min	0–30 min	30–60 min	0–30 min	30–60 min
Vehicle	±	±	±	±	±	±
0.1 μg/kg	±	±	±	±	±	±
1 μg/kg	±	±	±	±	±	±
10 μg/kg	±	±	↓(2)	±	↓(5)	±

±: No change, ↓: Decrease

The number in parentheses represents the number of mice exhibiting the abnormal behavior. (5 mice in each group.)

of the curves was extrapolated to infinity. Organ residence times were determined by calculating the area under the extrapolated time-activity curves with the trapezoidal method using WinNonlin version 1.5 software. The residence time of urinary bladder was calculated by applying the dynamic bladder model,[15] with a voiding interval of 4.8 hr (representing a rate of 5 times a day, typical of a normal adult). Residence times of GI tracts were calculated by applying the ICRP 30 GI tract model,[16] assuming that an activity passed through various segments of the GI tract at standard rates. Then using these residence times, organ absorbed doses and effective dose were estimated with the MIRDOSE 3.1 software package.[17]

Table 2 Effects of 5IA on respiratory rate (breaths/min)

	Baseline	1 min	2 min	3 min	5 min	15 min	30 min	45 min	60 min
Vehicle	104 ± 14	105 ± 20	108 ± 20	107 ± 16	113 ± 17	116 ± 19	118 ± 14	116 ± 9	111 ± 8
1 μg/kg	106 ± 16	113 ± 23	113 ± 17	114 ± 15	111 ± 14	114 ± 18	121 ± 21	119 ± 20	110 ± 18
2 μg/kg	111 ± 7	119 ± 16	117 ± 20	114 ± 30	116 ± 15	131 ± 15	125 ± 14	124 ± 14	120 ± 9
5 μg/kg	111 ± 4	162 ± 12#	150 ± 13#	144 ± 20#	141 ± 16#	138 ± 16#	138 ± 17#	128 ± 6*	126 ± 10

Values are mean ± s.d.
#$p < 0.01$, *$p < 0.05$ vs. Baseline.

Table 3 Effects of 5IA on heart rate (beats/min)

	Baseline	1 min	2 min	3 min	5 min	15 min	30 min	45 min	60 min
Vehicle	236 ± 16	227 ± 20	225 ± 16	236 ± 30	225 ± 21	221 ± 20	225 ± 17	224 ± 15	233 ± 26
1 μg/kg	230 ± 24	245 ± 17	242 ± 6	236 ± 15	243 ± 8	227 ± 6	234 ± 13	237 ± 12	233 ± 13
2 μg/kg	240 ± 8	252 ± 12	248 ± 23	240 ± 16	246 ± 19	254 ± 19	239 ± 13	236 ± 6	243 ± 8
5 μg/kg	251 ± 24	255 ± 26	255 ± 18	251 ± 19	257 ± 13	255 ± 12	255 ± 18	254 ± 10	263 ± 12

Values are mean ± s.d.
No significant change was observed in any group.

Table 4 Effects of 5IA on mean arterial blood pressure (% of baseline)

	Baseline	1 min	2 min	3 min	5 min	15 min	30 min	45 min	60 min
Vehicle	100	103 ± 2	105 ± 1	97 ± 6	91 ± 2	100 ± 5	104 ± 10	101 ± 11	100 ± 10
1 μg/kg	100	101 ± 6	106 ± 5	103 ± 11	104 ± 11	101 ± 14	103 ± 8	97 ± 4	94 ± 5
2 μg/kg	100	99 ± 2	99 ± 5	96 ± 16	99 ± 17	89 ± 11	94 ± 3	94 ± 7	91 ± 6
5 μg/kg	100	95 ± 3	94 ± 16	99 ± 11	102 ± 12	108 ± 8	99 ± 6	103 ± 5	112 ± 19

Values are mean ± s.d.
No significant change was observed in any group.

Table 5 Effects of 5IA on blood gas parameters

		Baseline	5 min	15 min	30 min	45 min	60 min
pH	Vehicle	7.43 ± 0.03	7.42 ± 0.03	7.42 ± 0.03	7.43 ± 0.02	7.42 ± 0.02	7.41 ± 0.01
	1 μg/kg	7.37 ± 0.03	7.37 ± 0.03	7.36 ± 0.02	7.37 ± 0.02	7.37 ± 0.02	7.36 ± 0.04
	2 μg/kg	7.37 ± 0.02	7.35 ± 0.02	7.36 ± 0.02	7.35 ± 0.03	7.35 ± 0.03	7.36 ± 0.04
	5 μg/kg	7.39 ± 0.06	7.36 ± 0.05	7.37 ± 0.04	7.37 ± 0.04	7.38 ± 0.03	7.38 ± 0.04
PCO_2 (mmHg)	Vehicle	48.0 ± 6.7	48.4 ± 6.1	49.0 ± 7.0	45.7 ± 2.6	44.9 ± 1.8	45.1 ± 1.5
	1 μg/kg	44.8 ± 1.9	44.3 ± 3.2	46.3 ± 2.0	45.6 ± 1.8	44.9 ± 3.7	44.1 ± 2.9
	2 μg/kg	50.4 ± 5.7	53.5 ± 9.9	48.9 ± 3.6	46.6 ± 3.7	44.5 ± 4.4	43.6 ± 6.4*
	5 μg/kg	48.0 ± 3.3	50.0 ± 2.7	48.4 ± 3.5	45.8 ± 2.8	44.9 ± 1.4	43.7 ± 2.0
PO_2 (mmHg)	Vehicle	74.6 ± 5.1	75.0 ± 2.4	76.4 ± 4.6	75.4 ± 5.0	77.9 ± 5.5	79.0 ± 3.3
	1 μg/kg	80.5 ± 6.5	78.4 ± 8.7	80.3 ± 8.4	80.8 ± 7.3	80.2 ± 7.9	78.9 ± 5.9
	2 μg/kg	77.9 ± 9.2	72.2 ± 2.5	76.1 ± 4.2	81.3 ± 4.3	80.3 ± 9.8	83.0 ± 5.9
	5 μg/kg	75.8 ± 6.9	71.2 ± 9.3	76.3 ± 4.5	79.0 ± 3.6	79.6 ± 2.8	83.7 ± 0.3*

Values are mean ± s.d. *$p < 0.05$ vs. Baseline.

Brain SPECT

Brain SPECT was performed at 4 hr after the administration of 171 MBq of [^{123}I]5IA. The subject received Lugol's solution (containing 400 mg of potassium iodide) orally 30 min prior to receiving [^{123}I]5IA. SPECT images were acquired for 20 min with a three-headed rotating gamma camera system (PRISM 3000, Picker International, Inc., USA) equipped with low-energy, high resolution, fanbeam collimators. This system provided a spatial resolution of 8.0 mm full-width at half-maximum (FWHM) at the center of the field of view with a sensitivity of 135 cps/MBq.

All SPECT images were filtered with a Butterworth filter (cutoff frequency, 0.25; order, 4) and reconstructed using a filtered backprojection algorithm with a ramp filter. Attenuation correction was performed using the ellipses outer line approximation and Chang's method (coefficient of 0.06/cm), which assumes that the attenuation process is homogeneous throughout the brain and can be described by an exponential function.

RESULTS

Behavior

In all three dose groups tested (0.1 μg/kg, 1 μg/kg, and 10 μg/kg), no changes were observed in the righting reflex or motor functions such as grip, walking and tonus of muscle in mice after administration of 5IA. No changes in spontaneous locomotion or grooming were noted in the animals administered 1 μg/kg of 5IA or less. In the 10 μg/kg treated group, decreases in spontaneous locomotion (5 mice in 5 mice) and grooming (2 mice in 5 mice) were observed 0–30 min after 5IA administration, but this sedative effect was transient and disappeared within 30 min post-administration (Table 1).

No significant difference was observed in body weight among control or 5IA-treated groups at 7 days after drug administration. This suggests that at 10 μg/kg or less, 5IA has no sub-acute toxicity (Fig. 1).

Physiological parameters

The administration of 5 μg/kg of 5IA immediately resulted in a significant increase in the respiratory rate (111 ± 4 breaths/min at baseline and 162 ± 12 breaths/min at 1 min), and this increase was significant until 45 min (128 ± 6 breaths/min at 45 min). The administration of 2 μg/kg also tended to increase the respiratory rate, although not significantly (111 ± 7 at baseline, 119 ± 16 at 1 min and 131 ± 15 at 15 min). On the other hand, no significant changes were noted in the group treated with vehicle or 1 μg/kg of 5IA (Table 2). Heart rate averaged 236 ± 16 beats/min in the vehicle-treated group with no significant difference from the values for the three groups treated with 5IA (Table 3). In rats administered a dose of 5 μg/kg or less, 5IA did not produce any changes in mean arterial blood pressure (MABP) (74 ± 12 mmHg at basal and

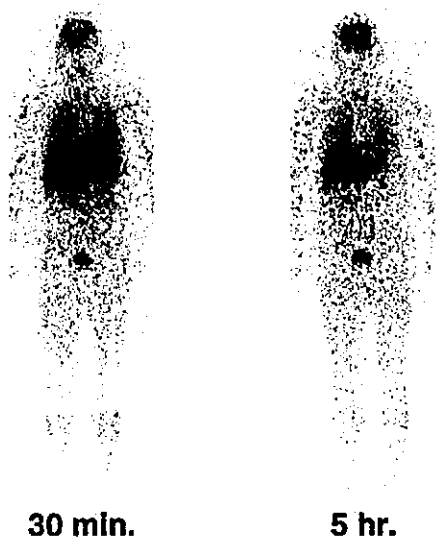

Fig. 2 Typical anterior whole-body images 30 min and 5 hr after the intravenous administration of [^{123}I]5IA. Brain, lungs, liver and bladder were clearly visualized in both images.

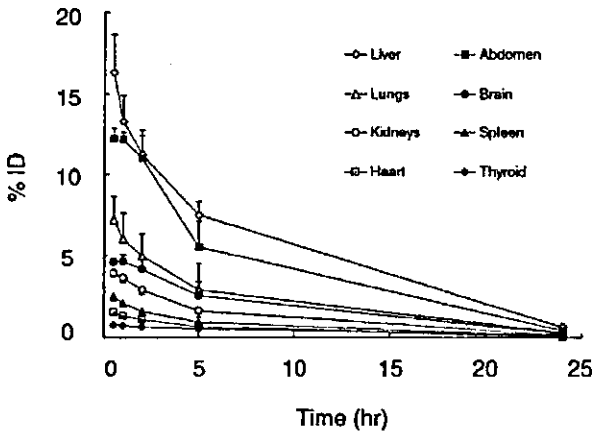

Fig. 3 Time-activity curves for various organs. Data were not corrected for decay and are expressed as percent injected radioactivity of [^{123}I]5IA. Each point represents the mean ± s.d. for all subjects.

Table 6 Mean residence times for all subjects

	Residence time (hr)
Liver	1.36 ± 0.15
Urinary bladder content	1.24 ± 0.30
Upper large intestine	0.79 ± 0.04
Lower large intestine	0.64 ± 0.03
Lungs	0.56 ± 0.28
Brain	0.47 ± 0.14
Small intestine	0.41 ± 0.02
Kidneys	0.31 ± 0.06
Spleen	0.18 ± 0.01
Thyroid	0.14 ± 0.06
Rest of body	4.57 ± 1.29

Values are the mean ± s.d.

91–105%, 94–106%, 89–100%, and 94–112% of baseline during 60 min after administration of vehicle, 1 μg/kg, 2 μg/kg, and 5 μg/kg, respectively) (Table 4). Rats administered 100 μg/kg of 5IA showed transient increases in both heart rate and MABP.

No changes in blood pH or blood gases were noted in the animals administered 1 μg/kg of 5IA. In rats administered 2 μg/kg and 5 μg/kg of 5IA, PCO_2 tended to decrease and PO_2 tended to increase at 60 min after injection (Table 5).

Biodistribution

Serial whole-body images of [^{123}I]5IA are shown in Figure 2. The temporal distribution profiles of the radioactivity in various organs are shown in Figure 3. At 30 min after injection, high levels of radioactivity were accumulated in the liver and urinary bladder, and moderate levels in the lungs, kidneys and brain. The radioactivity in the liver and lungs was rapidly eliminated. Penetration of the blood-brain barrier peaked at 1 hr after administration and was followed by a gradual decrease. The radioactivity in the kidneys decreased gradually with time. A small amount of radioactivity was observed in the thyroid. Twenty-four hours after injection, less than 1% of the injected radioactivity remained in any organs. The biological half-life of [^{123}I]5IA averaged 7.2 ± 4.0 hr.

The radioactivity in the urinary bladder increased rapidly, indicating prompt excretion through the renal system. The mean measured urinary excretion 24 hr after injection was 74 ± 4%. No clear evidence of biliary excretion was seen on the images. Furthermore, the administration of [^{123}I]5IA did not cause any changes in blood, liver, or urine parameters.

Table 7 Radiation dose estimates for [^{123}I]5IA

Target organ	Absorbed dose (μGy/MBq)
Thyroid	145 ± 61
Urinary bladder wall	98 ± 21
Lower large intestine wall	63 ± 2.7
Upper large intestine wall	54 ± 2.3
Kidneys	35 ± 5.8
Spleen	32 ± 2.3
Liver	32 ± 2.9
Small intestine	25 ± 1.2
Lungs	18 ± 7.4
Ovaries	18 ± 0.9
Uterus	17 ± 0.8
Gallbladder wall	15 ± 1.2
Heart wall	15 ± 3.7
Brain	14 ± 4.2
Bone surfaces	11 ± 2.2
Pancreas	10 ± 1.5
Adrenals	10 ± 1.6
Total body	8.6 ± 1.2
Stomach	8.6 ± 1.4
Red marrow	6.9 ± 1.1
Muscle	6.7 ± 1.0
Testes	6.3 ± 0.6
Thymus	5.6 ± 1.6
Breasts	4.3 ± 1.2
Skin	3.8 ± 0.8
Effective dose equivalent*	30 ± 1.4
Effective dose*	32 ± 2.6

Values are the mean ± s.d. *Units are μSv/MBq.

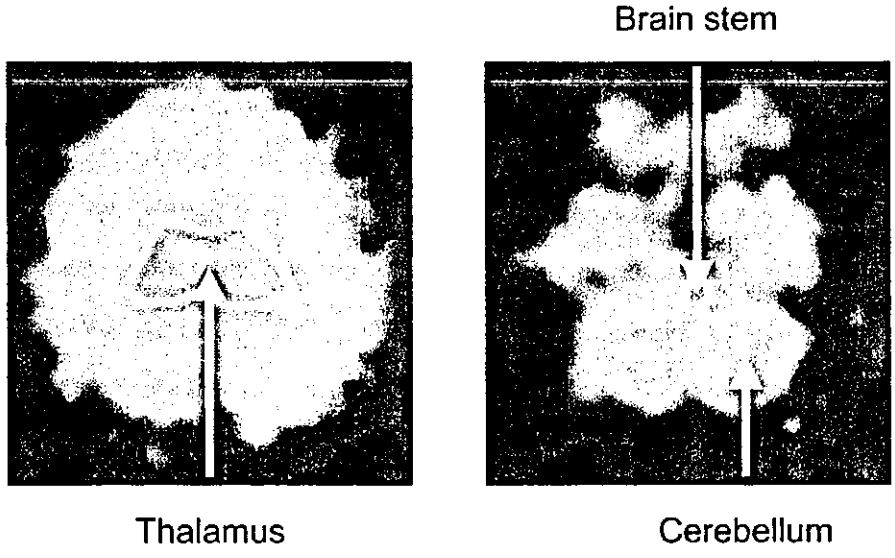

Fig. 4 SPECT images acquired 4 hr after administration of [^{123}I]5IA. The distribution of [^{123}I]5IA was associated with the known distribution of nAChR in human brain (thalamus > brain stem > cerebellum > cortex).

Dosimetry

Table 6 shows mean residence times for three subjects calculated from the time-activity curves. The residence times for urinary bladder content were calculated using the dynamic bladder model and those for the intestinal tracts, using the GI tract model. The dataset of each subject was fitted independently. The residence time was highest for the rest of body, followed by the liver and the urinary bladder. From these data and the biological half-lives of each subject, radiation absorbed doses were estimated using the MIRDOSE 3.1 software and the mean values obtained are shown in Table 7.

The highest radiation dose was to the thyroid, followed by the urinary bladder wall, lower large intestine wall and upper large intestine wall. The effective dose equivalent was 30 ± 1 μSv/MBq.

Brain SPECT

The SPECT image obtained 4 hr after the administration of [^{123}I]5IA revealed the highest uptake of radioactivity to be in the thalamus. The radioactivity in the brain stem and the cerebellum was greater than that in the cerebral cortices (Fig. 4).

DISCUSSION

The safety of a radioligand is determined by both its toxicity and radiation.

Since the righting reflex remained unchanged and grip, walking and tonus of muscle were normal in mice administered 10 μg/kg of 5IA or less, 5IA had no effect on motor functions or static senses at 10 μg/kg or less. On the other hand, transient decreases in spontaneous locomotion were observed in all mice administered 10 μg/kg of 5IA. The inhibitory effect on the central nervous system seems to be responsible for this finding, since motor dysfunctions were not observed at this dose. Thus, since no abnormal behavior was observed at 1 μg/kg or less, the NOEL of 5IA was 1 μg/kg.

The experiments on physiological parameters demonstrated that the respiratory rate tended to increase in rats injected with 2 μg/kg and 5 μg/kg of 5IA. Since nicotine has also been reported to increase the respiratory rate,[18] the effect of 5IA on respiration may be mediated by nAChR. The respiratory rate, cardiovascular parameters and blood gas parameters were not changed from the baseline in the 1 μg/kg-treated group. Therefore, the experiments on physiological parameters also indicated that the NOEL was 1 μg/kg. Given that an epibatidine analogue was lethal (30%) at an intravenous dose of 1.5 μg/kg,[19] 5IA has a greatly reduced toxicity profile. The lower toxicity of 5IA might be associated with its low affinity for the $\alpha 3\beta 4$ subtype, to which epibatidine binds with high affinity.[20,21]

The specific radioactivity of [^{123}I]5IA is important to determine the chemical mass of 5IA to be administered. In the present study, a very high specific radioactivity of more than 169 GBq/μmol was obtained. Based on the uptake of [^{123}I]5IA by the brain, we estimated that 185 MBq of [^{123}I]5IA would be sufficient for SPECT imaging in humans. In this case, the chemical mass of [^{123}I]5IA corresponds to less than 5.3 ng/kg (18.2 pmol/kg) for a 60 kg individual (total dose; 0.32 μg), which is about 190 times lower than the NOEL and about 230,000 times lower than the LD_{50} (4.2 μmol/kg).[22] Thus, these results would support the utilization of [^{123}I]5IA in human nAChR imaging.

From the point of view of radiation protection, another factor determining the safety of a radioligand, the radiation dose of [^{123}I]5IA was estimated from whole-body images. Following injection of [^{123}I]5IA, the majority (~75%) of the radioactivity was excreted in urine 24 hr after administration, demonstrating that [^{123}I]5IA is mainly cleared from the renal system. The biological half-life of [^{123}I]5IA averaged 7.2 hr. Based on the biodistribution data, the effective dose equivalent was calculated to be 30 μSv/MBq. This value is in agreement with the results of another group[23] and lower than that of other ^{123}I-labeled receptor imaging ligands such as [^{123}I]IBF (41 μSv/MBq)[24] and [^{123}I]iodo-PK 11195 (40 μSv/MBq).[25] On the other hand, the administration of 171 MBq of [^{123}I]5IA (0.0049 μg/kg) clearly revealed a regional SPECT image which is consistent with the distribution of nAChR in human brain[2]; that is, the level of radioactivity was highest in the thalamus, high in the brain stem, moderate in the cerebellum and low in the cortical area. So, even if 185 MBq of [^{123}I]5IA is administered, the effective dose equivalent is estimated to be 5.6 mSv, which is almost the same as the average effective dose equivalent per patient from nuclear medicine (5 mSv).[26] Thus, the use of up to 185 MBq of [^{123}I]5IA may be adequate for SPECT imaging of nAChR in humans.

The highest absorbed dose was estimated in the thyroid based on whole-body imaging. This result indicates the necessity for thyroid blockade by the administration of Lugol's solution before the use of [^{123}I]5IA.

In conclusion, the NOEL of 5IA was 1 μg/kg and therefore, it is predicted that [^{123}I]5IA injected at the usual clinical dose would have no pharmacological effect. In addition, the radiation absorbed dose estimated based on the results of whole-body imaging appeared acceptable for clinical SPECT imaging. Furthermore, the regional distribution of radioactivity in the image of human brain was associated with the known nAChR distribution. These results highlight the promise of [^{123}I]5IA as a ligand for the SPECT imaging of nAChR in humans.

ACKNOWLEDGMENTS

This work was supported in part by a grant-in-aid for Scientific Research from the Ministry of Education, Science and Technology of Japan, a grant from 21st Century COE program

"Knowledge Information Infrastructure for Genome Science" and a grant from the Smoking Research Foundation. The authors thank Nihon Medi-Physics Co. Ltd. for providing sodium [^{123}I]iodine.

REFERENCES

1. Gotti C, Fornasari D, Clementi F. Human neuronal nicotinic receptors. *Prog Neurobiol* 1997; 53: 199–237.
2. Paterson D, Nordberg A. Neuronal nicotinic receptors in the human brain. *Prog Neurobiol* 2000; 61: 75–111.
3. Akaike A, Tamura Y, Yokota T, Shimohama S, Kimura J. Nicotine-induced protection of cultured cortical neurons against *N*-methyl-D-aspartate receptor-mediated glutamate cytotoxicity. *Brain Res* 1994; 644: 181–187.
4. Holladay MW, Bai H, Li Y, Lin NH, Daanen JF, Ryther KB, et al. Structure-activity studies related to ABT-594, a potent nonopioid analgesic agent: effect of pyridine and azetidine ring substitutions on nicotinic acetylcholine receptor binding affinity and analgesic activity in mice. *Bioorg Med Chem Lett* 1998; 8: 2797–2802.
5. Burghaus L, Schutz U, Krempel U, de Vos RA, Jansen Steur EN, Wevers A, et al. Quantitative assessment of nicotinic acetylcholine receptor proteins in the cerebral cortex of Alzheimer patients. *Brain Res Mol Brain Res* 2000; 76: 385–388.
6. Shimohama S, Taniguchi T, Fujiwara M, Kameyama M. Changes in nicotinic and muscarinic cholinergic receptors in Alzheimer-type dementia. *J Neurochem* 1986; 46: 288–293.
7. Burghaus L, Schutz U, Krempel U, Lindstrom J, Schroder H. Loss of nicotinic acetylcholine receptor subunits alpha4 and alpha7 in the cerebral cortex of Parkinson patients. *Parkinsonism Relat Disord* 2003; 9: 243–246.
8. Guan ZZ, Nordberg A, Mousavi M, Rinne JO, Hellstrom-Lindahl E. Selective changes in the levels of nicotinic acetylcholine receptor protein and of corresponding mRNA species in the brains of patients with Parkinson's disease. *Brain Res* 2002; 956: 358–366.
9. Chefer SI, Horti AG, Lee KS, Koren AO, Jones DW, Gorey JG, et al. *In vivo* imaging of brain nicotinic acetylcholine receptors with 5-[^{123}I]iodo-A-85380 using single photon emission computed tomography. *Life Sci* 1998; 63: PL355–360.
10. Fujita M, Tamagnan G, Zoghbi SS, Al-Tikriti MS, Baldwin RM, Seibyl JP, et al. Measurement of alpha4beta2 nicotinic acetylcholine receptors with [^{123}I]5-I-A-85380 SPECT. *J Nucl Med* 2000; 41: 1552–1560.
11. Musachio JL, Scheffel U, Finley PA, Zhan Y, Mochizuki T, Wagner HN Jr, et al. 5-[I-125/123]Iodo-3(2(*S*)-azetidinylmethoxy)pyridine, a radioiodinated analog of A-85380 for *in vivo* studies of central nicotinic acetylcholine receptors. *Life Sci* 1998; 62: PL351–357.
12. Musachio JL, Villemagne VL, Scheffel UA, Dannals RF, Dogan AS, Yokoi F, et al. Synthesis of an I-123 analog of A-85380 and preliminary SPECT imaging of nicotinic receptors in baboon. *Nucl Med Biol* 1999; 26: 201–207.
13. Saji H, Ogawa M, Ueda M, Iida Y, Magata Y, Tominaga A, et al. Evaluation of radioiodinated 5-iodo-3-(2(*S*)-azetidinylmethoxy)pyridine as a ligand for SPECT investigations of brain nicotinic acetylcholine receptors. *Ann Nucl Med* 2002; 16: 189–200.
14. United States Government. Single dose acute toxicity testing for pharmaceuticals. *Federal Register* 1996; 61: 43934–43935.
15. Cloutier RJ, Smith SA, Watson EE, Snyder WS, Warner GG. Dose to the fetus from radionuclides in the bladder. *Health Phys* 1973; 25: 147–161.
16. International Commission on Radiological Protection. *Limits for intakes of radionuclides by workers*. New York; Pergamon Press, 1979.
17. Stabin MG. MIRDOSE: personal computer software for internal dose assessment in nuclear medicine. *J Nucl Med* 1996; 37: 538–546.
18. Volle RL, Koelle GB. Ganglionic stimulating and blocking agents. In: *The Pharmacological Basis of Therapeutics*, Goodman LS, Gilman A (eds), New York; The Macmillan Company, 1970: 585–600.
19. Molina PE, Ding YS, Carroll FI, Liang F, Volkow ND, Pappas N, et al. Fluoro-norchloroepibatidine: preclinical assessment of acute toxicity. *Nucl Med Biol* 1997; 24: 743–747.
20. Stauderman KA, Mahaffy LS, Akong M, Velicelebi G, Chavez-Noriega LE, Crona JH, et al. Characterization of human recombinant neuronal nicotinic acetylcholine receptor subunit combinations alpha2beta4, alpha3beta4 and alpha4beta4 stably expressed in HEK293 cells. *J Pharmacol Exp Ther* 1998; 284: 777–789.
21. Xiao Y, Meyer EL, Thompson JM, Surin A, Wroblewski J, Kellar KJ. Rat alpha3/beta4 subtype of neuronal nicotinic acetylcholine receptor stably expressed in a transfected cell line: pharmacology of ligand binding and function. *Mol Pharmacol* 1998; 54: 322–333.
22. Sihver W, Nordberg A, Langstrom B, Mukhin AG, Koren AO, Kimes AS, et al. Development of ligands for *in vivo* imaging of cerebral nicotinic receptors. *Behav Brain Res* 2000; 113: 143–157.
23. Fujita M, Seibyl JP, Vaupel DB, Tamagnan G, Early M, Zoghbi SS, et al. Whole-body biodistribution, radiation absorbed dose, and brain SPET imaging with [^{123}I]5-I-A-85380 in healthy human subjects. *Eur J Nucl Med Mol Imaging* 2002; 29: 183–190.
24. van Dyck CH, Seibyl JP, Stubbs JB, Zoghbi S, Wisniewski G, Baldwin RM, et al. Human biodistribution and dosimetry of the SPECT D_2 dopamine receptor radioligand [^{123}I]IBF. *Nucl Med Biol* 1996; 23: 9–16.
25. Versijpt J, Dumont F, Thierens H, Jansen H, De Vos F, Slegers G, et al. Biodistribution and dosimetry of [^{123}I]iodo-PK 11195: a potential agent for SPET imaging of the peripheral benzodiazepine receptor. *Eur J Nucl Med* 2000; 27: 1326–1333.
26. Beekhuis H. Population radiation absorbed dose from nuclear medicine procedures in The Netherlands. *Health Phys* 1988; 54: 287–291.

Cerebral atrophy and its relation to cognitive impairment in Parkinson disease

A. Nagano-Saito, MD, PhD; Y. Washimi, MD, PhD; Y. Arahata, MD, PhD; T. Kachi, MD, PhD; J.P. Lerch, BA; A.C. Evans, PhD; A. Dagher, MD; and K. Ito, MD, PhD

Abstract—*Objective:* Voxel-based morphometry was used to compare the amounts of gray matter in the brains of patients with Parkinson disease (PD) and normal control subjects (NCs) and to identify the specific regions responsible for cognitive dysfunction in PD. *Methods:* Patients were classified into nondemented (ND) and demented (D) groups according to the criteria of the Diagnostic and Statistical Manual of Mental Disorders (4th ed.), and a group comparison was performed. In the ND patients, a correlation was also performed between local gray matter density and the score on Raven Colored Progressive Matrices (RCPM), a test of executive and visuospatial function. *Results:* In patients with advanced ND-PD vs NCs, atrophic changes were observed in the limbic/paralimbic areas and the prefrontal cortex. In D vs ND patients, atrophic change was observed widely in the limbic/paralimbic system, including the anterior cingulate gyrus and hippocampus as well as the temporal lobe, dorsolateral prefrontal cortex, thalamus, and caudate nucleus. The RCPM score was positively correlated with the gray matter density in the dorsolateral prefrontal cortex and the parahippocampal gyrus. *Conclusions:* In patients with Parkinson disease (PD), atrophic changes occur mainly in the limbic/paralimbic and prefrontal areas. These atrophic changes may be related to the development of dementia in PD.

NEUROLOGY 2005;64:224–229

Cognitive impairment is relatively frequent in Parkinson disease (PD), especially at an advanced stage. In its severe form, it may be global and meet the Diagnostic and Statistical Manual of Mental Disorders (4th ed.; DSM- IV) criteria for dementia.[1] The prevalence of dementia in PD is estimated to be 20 to 40%.[1,2] Moreover, even in the absence of dementia, specific impairments in executive function, visual memory, and visuospatial abilities are often present.[3,4] Raven Colored Progressive Matrices (RCPM), which was initially developed as a nonverbal intellectual test,[5] has been shown to be sensitive to cognitive deficits in PD[6] and can be considered to rely on at least two cognitive factors: visuospatial and executive functions.[7]

A small number of MRI studies have related brain atrophy to cognitive dysfunction in PD. There have been reports, among nondemented PD (ND-PD) patients, of major correlations between verbal learning or frontal lobe function scores and ventricular enlargement[8] and between annual reductions in brain volume and reductions in performance and full-scale IQ.[9] In another study of ND-PD patients, hippocampal atrophy was found to correlate with memory impairment.[10] Finally, reduced gray matter volume in demented PD (D-PD) patients was observed in widespread cortical (temporal, occipital, lateral prefrontal) and subcortical (caudate, putamen, thalamus) areas vs control subjects using voxel-based morphometry (VBM).[11] However, as far as we know, there have been no reports on the relation between gray matter atrophy and cognitive impairment in ND-PD using VBM.

The aim of this study was to identify the gray matter atrophic changes that are associated with specific cognitive impairment and dementia in PD. We used VBM to assess focal brain atrophy in the whole brain of PD patients with and without dementia and matched healthy control subjects. We also correlated gray matter density to performance on the RCPM in the ND-PD patients.

Methods. *Subjects.* Fifty-eight patients with PD who fulfilled the clinical criteria for the diagnosis of PD[12] were recruited. Detailed interview with patients and their families and neurologic examination were used to determine cognitive status. Nine patients were diagnosed as D-PD according to the DSM-IV criteria. All of them had impairments in memory function affecting their daily life and had experienced visual hallucinations. One patient had cognitive fluctuation and, as a result, also fulfilled the criteria of the Consortium on Dementia with Lewy Bodies International Workshop.[13] In all D-PD, the onset of parkinsonism preceded the development of dementia by at least 2 years, and significant cognitive impairment involving executive function and/or visuospatial abilities preceded the memory difficulties. Among the

From Department of Neurology (Drs. Nagano-Saito, Washimi, Arahata, and Kachi), National Hospital for Geriatric Medicine, and Department of Brain Science and Molecular Imaging (Dr. Ito), National Institute for Longevity Sciences, National Center for Geriatrics and Gerontology, Obu, Japan; and McConnell Brain Imaging Centre (Drs. Nagano-Saito, Lerch, Evans, and Dagher), Montreal Neurological Institute, McGill University, Montreal, Quebec, Canada.

Supported by funds for Research on Health Science of Mind of Aging and Health from the Ministry and Welfare of Japan.

Received May 20, 2004. Accepted in final form September 29, 2004.

Address correspondence and reprint requests to Dr. Y. Arahata, Department of Neurology, National Center for Geriatrics and Gerontology, 36-3 Gengo, Morioka, Obu, Aichi, Japan 474-8511; e-mail: arahatay@nils.go.jp

Table 1 Clinical features of normal subjects and patients

Group category	Comparison	No.	Age, y	H-Y Scale	UPDRS motor score	Disease duration, y	MMSE score
NC	NC vs all ND-PD NC vs advanced ND-PD	31	63.5 ± 8.8				29.2 ± 1.2
ND-PD	NC vs all ND-PD	39	61.8 ± 8.1	2.3 ± 0.9	25.5 ± 16.1	3.5 ± 3.4	28.4 ± 1.9
	NC vs advanced ND-PD	19	62.6 ± 7.9	3.1 ± 0.5	37.4 ± 15.3	4.9 ± 4.3	28.1 ± 2.0
	Advanced ND-PD vs D-PD	17	65.4 ± 6.4	3.1 ± 0.6	38.7 ± 15.7	5.2 ± 4.5	27.9 ± 2.0
	Regression analysis	38	61.9 ± 8.2	2.3 ± 0.9	26.0 ± 16.0	3.6 ± 3.4	28.4 ± 1.9
D-PD	ND-PD vs D-PD	9	67.3 ± 5.4	3.3 ± 0.7	45.7 ± 10.9*	9.3 ± 5.4	16.1 ± 5.7

* n = 8.

H-Y = Hoehn and Yahr; UPDRS = Unified Parkinson's Disease Rating Scale; MMSE = Mini-Mental State Examination; NC = normal control; ND-PD = nondemented Parkinson disease; D-PD = demented Parkinson disease.

remaining PD patients, none fulfilled the DSM-IV criteria for delirium or amnesic disorder. After excluding patients with a history of hallucination, severe depression, severe autonomic failure, or resistance to dopaminergic medications, 39 PD patients remained to form the ND-PD group. All patients were rated using the Hoehn and Yahr (H-Y) Scale and the Mini-Mental State Examination (MMSE). All patients except three D-PD patients were rated using the Unified Parkinson's Disease Rating Scale (UPDRS), and all ND-PD patients except one underwent the RCPM Test. Thirty-one normal control subjects (NCs), who were neurologically intact and age matched to the ND-PD patients, were also recruited. Permission to perform these studies was obtained from the Ethical Committee of the National Center for Geriatrics and Gerontology.

MRI and VBM. High-resolution volumetric MRI was performed on a 1.5 T Visart MRI scanner (Toshiba, Tokyo, Japan) using a three-dimensional field echo sequence (repetition time 20 milliseconds, echo time 7 milliseconds, flip angle 35°), generating T1-weighted contiguous sagittal slices with a pixel size of 0.89 × 0.89 mm and a slice thickness of 1.3 mm. These T1-weighted brain volumes were linearly transformed into stereotaxic space using nine parameters[14] to match the Montreal Neurologic Institute template with a voxel size of 1 × 1 × 1 mm. The volumes also underwent a nonuniformity correction[15] to remove variations in signal intensity related to radiofrequency inhomogeneity. With use of the individual parameters of the linear transformation, the images were transformed into the standardized stereotaxic space. The transformed images were then classified into gray matter, white matter, and CSF using an automatic tissue classification algorithm.[16] Mask images were generated from the individual spatially transformed images to remove the skull and dura.[17] With use of the tissue-classified and mask images, probability images of gray matter were created using an algorithm that estimates the relative amount of gray and white matter, CSF, and background in each voxel.[18] These gray matter probability images were then blurred with an isotropic Gaussian kernel (full width at half-maximum = 8 mm). Statistical analyses were performed on the blurred gray matter probability images.

Statistical analysis. Four voxel-based statistical analyses were performed as follows: 1) group comparison between 31 NCs and 39 ND-PD patients, 2) group comparison between 31 NCs and 19 advanced ND-PD patients (defined as H-Y score of >2), 3) group comparison between 17 advanced ND-PD and 9 D-PD patients, and 4) regression analysis between the RCPM scores and the gray matter probability maps of 38 ND-PD patients. In the third comparison, patients matched to the D-PD patients for age and H-Y score were selected from the advanced ND-PD group. Because these two groups could not be matched for disease duration, this subtraction was also carried out with disease duration as a confounding covariate.

The effect of each comparison was tested, and the result was indicated as a T map. Random field theory was used to assign a p value to each cluster based on its height and extent.[19] The degrees of freedom for each comparison were set to the number of subject scans used minus 2. Clusters with a height threshold set at $p < 0.001$ and an extent threshold set at corrected $p < 0.05$ were considered significant.

Results. The number, mean age, disease duration, H-Y score, UPDRS motor score, and MMSE score for each group of each comparison are shown in table 1. No significant differences were observed in mean age, H-Y score, or UPDRS motor score in any group comparisons. There was, however, a trend toward longer disease duration in the D-PD group vs the ND-PD group. There were no significant differences in dosages of any antiparkinsonian medication between advanced ND-PD and D-PD groups. The RCPM score ranged from 20 to 36 (mean 30.0 ± 4.4). There was no correlation between the UPDRS motor scores and the RCPM scores in ND-PD patients (correlation coefficient −0.02, $p = 0.93$).

There were no differences in gray matter density between the ND-PD and NC groups. In the advanced ND-PD group vs NCs, there were atrophic changes in the bilateral straight gyrus extending into the subcallosal gyrus, Brodmann area (BA) 11/25, left inferior frontal gyrus (ventrolateral prefrontal cortex, BA 44), and left parahippocampal gyrus (BA 30) (figure 1). In the D-PD group vs matched ND-PD patients, there were atrophic changes in the bilat-

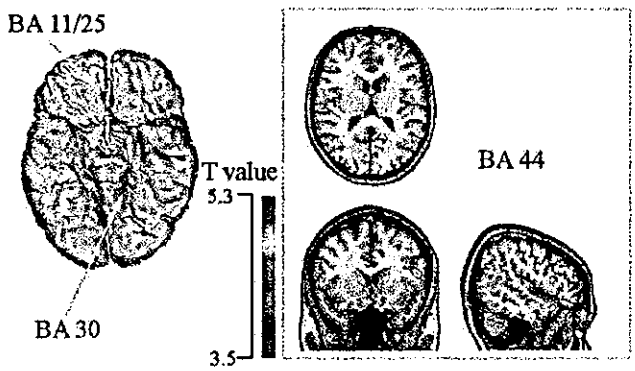

Figure 1. Regions with significant difference between normal control subject and nondemented patient with advanced Parkinson disease. The T value with 3.5 and above is superimposed on the template MRI. The right side of each axial and coronal figure corresponds with the right side of the brain. BA = Brodmann area.

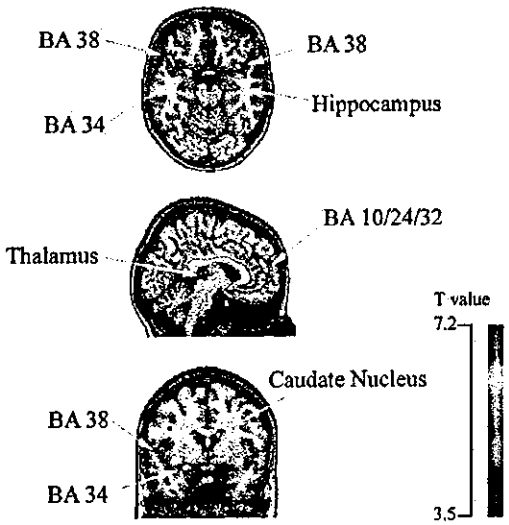

Figure 2. Regions with significant difference between advanced Parkinson disease without dementia and Parkinson disease with dementia. The T value with 3.5 and above is superimposed on the template MRI. The right side of each axial and coronal figure corresponds with the right side of the brain. BA = Brodmann area.

eral anterior cingulate gyrus extending to the medial frontal gyrus (BA 10/24/32), bilateral parahippocampal gyrus (BA 34), bilateral anterior part of the superior temporal gyrus, corresponding to the temporal operculum, extending to the temporal polar region (BA 22/38), right hippocampus, right middle frontal gyrus (dorsolateral prefrontal cortex, BA 46), bilateral caudate nuclei, and left thalamus (figure 2). These results were essentially unaffected when disease duration was covaried out (table 2). In ND-PD patients, the RCPM score was positively correlated with the gray matter density in the right parahippocampal/fusiform gyrus (BA 37), left parahippocampal gyrus (BA 19/28), left superior frontal gyrus (BA 10), and right middle frontal gyrus (dorsolateral prefrontal cortex, BA 9) (figure 3). Table 2 lists the peaks of the most significant differences in these results.

Discussion. *NCs vs ND-PD patients.* In the ND-PD group as a whole, no loss of gray matter was observed vs NC, and this result is consistent with previous MRI studies.[20,21] In contrast, the advanced ND-PD patients showed gray matter loss in three areas vs NCs: straight gyrus, inferior frontal gyrus, and parahippocampal gyrus. The straight gyrus, which is considered to be an extension of the anterior cingulate into the frontal lobe,[22] belongs to the paralimbic system, as does the parahippocampal gyrus. This finding is consistent with pathologic studies showing that the components of the limbic system are particularly vulnerable to degeneration in PD.[23] Mild pathologic change has also been observed in frontal association areas in PD,[23] and the atrophic change in the lateral prefrontal cortex observed in

***Table 2** List of peaks of most significant differences in comparisons*

Comparison	Region	Cluster				Coordinate		
		Voxels	*p* Corrected	Peak *T* value	Peak *T* value*	*x*	*y*	*z*
NC vs PD advanced	L rectal gyrus (BA 11/25)	1,143	<0.001	4.59		0	28	−26
	R inferior frontal gyrus (BA 44)	635	0.001	5.31		52	13	15
	L parahippocampal gyrus (BA 30)	380	0.026	4.3		−13	−40	−6
PD vs D-PD	L medial frontal gyrus (BA 10/24/32)	4,316	<0.001	7.21	6.82	−5	50	13
	L superior temporal gyrus (BA 38/22)	2,761	<0.001	5.34	5.11	−47	20	−18
	L parahippocampal gyrus (BA 34)	1,286	<0.001	6.75	5.84	−24	2	−16
	R caudate nucleus (body/head)	1,211	<0.001	4.82	4.72	12	1	18
	R superior temporal gyrus (BA 38/22)	1,034	<0.001	6.16	5.55	36	9	−17
	L thalamus	705	0.001	4.87	3.45	−7	−27	2
	R hippocampus	524	0.004	5.27	4.57	32	−17	−17
	L caudate nucleus (body/head)	464	0.007	4.39	4.33	−11	0	14
	R middle frontal gyrus (BA 46)	365	0.024	4.39	4.18	42	47	15
PD and RCPM	R parahippocampal/fusiform gyrus (BA 37)	678	0.001	5.01		27	−40	−14
	L superior frontal gyrus (BA 10)	611	0.002	6.07		−25	55	13
	L parahippocampal gyrus (BA 19)	511	0.005	4.63		−30	−56	−2
	R insula	509	0.005	4.74		38	11	2
	R middle frontal gyrus (BA 9)	441	0.011	5.39		45	8	37
	L parahippocampal gyrus (BA 28)	418	0.015	4.02		−22	−13	−14

* Peak *T* value with disease duration covaried out.

NC = normal control; PD = Parkinson disease; D-PD = demented Parkinson disease; RCPM = Raven Colored Progression Matrices; BA = Brodmann area.

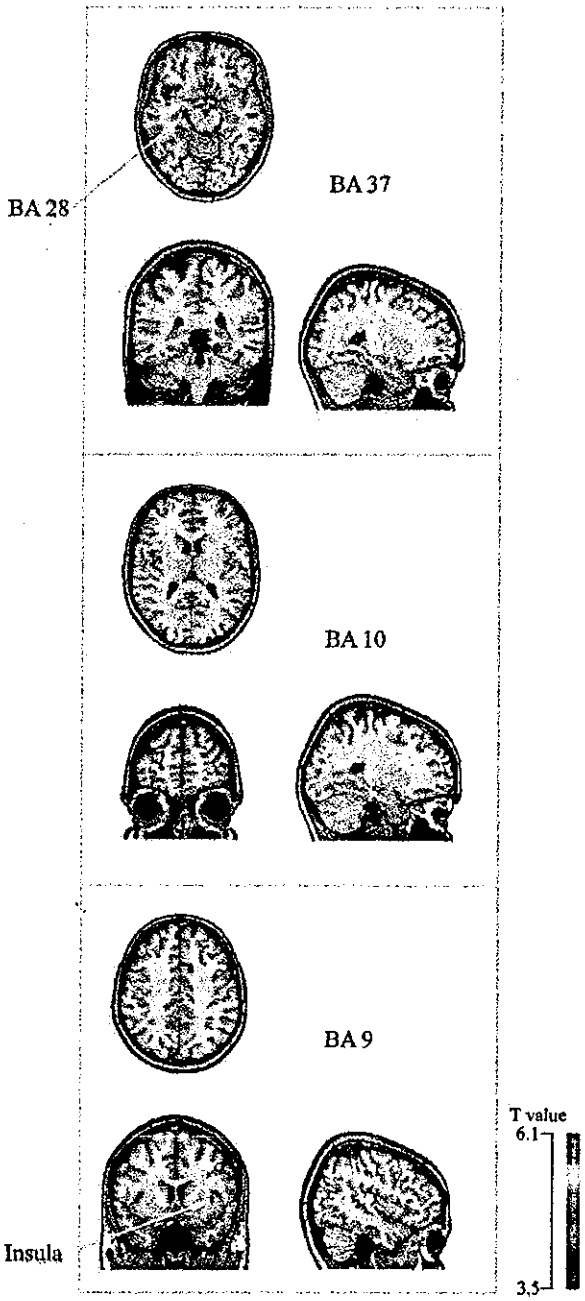

Figure 3. Region with significantly positive correlation to the Raven Colored Progressive Matrices score. The T *value with 3.5 and above is superimposed on the template MRI. The right side of each axial and coronal figure corresponds with the right side of the brain. BA = Brodmann area.*

our study in advanced PD patients likely reflects intrinsic frontal lobe degeneration.

ND-PD vs D-PD patients. When we compared D-PD patients with a group of ND-PD patients matched for motor disability, we observed widespread atrophic changes in the limbic/paralimbic system. We selected D-PD patients according to the DSM-IV criteria, which require memory impairment. Thus, our finding of atrophy involving the Papez circuit, which is strongly implicated in memory, likely accounts for the memory impairment in our group of D-PD patients. Pathologic studies have implicated the medial temporal lobe in dementia in PD. Demented patients have higher densities of parahippocampal Lewy bodies on pathologic examination,[24] and there have been reports of correlations between clinical dementia severity and the number of Lewy bodies in the entorhinal cortex[25] and the density of Lewy neurites in the CA2 field of the hippocampus.[26] Moreover, previous MRI studies indicated that hippocampal atrophy is related to impaired memory in ND-PD patients.[10,27] We conclude that atrophy of the hippocampus and parahippocampal gyrus may be an important determinant of dementia in PD.

Within the limbic/paralimbic system, the strongest difference in gray matter between the ND-PD and D-PD patients was observed in the anterior cingulate gyrus extending into the medial frontal gyrus. The anterior cingulate cortex is one of the cortical areas showing the greatest concentration of Lewy bodies in PD,[23,24,28] and a significant correlation has been reported between Clinical Dementia Rating Scale score and Lewy body density in this region.[25] Neuroimaging studies have implicated the anterior cingulate gyrus in attention[29] and in a variety of tasks that require high-level cognitive processing.[30] Thus, the loss of gray matter in the anterior cingulate gyrus may be related to the impairment in the ability to spontaneously generate efficient cognitive strategies in patients with PD.[31]

In a previous PET study, we described a decrease in the 6-[^{18}F] fluoro-L-dopa influx rate constant in the anterior cingulate in D-PD vs ND-PD.[32] It is possible that the loss of gray matter in the anterior cingulate described in the current study includes the loss of mesolimbic dopaminergic projections to the area. However, anterior cingulate atrophy would likely also cause partial volume effects that could have accounted for our previous result.

Reduced gray matter density was also observed in the thalamus and caudate in D-PD patients. These subcortical atrophic changes are consistent with a previous pathologic study in D-PD patients[33] and two recent VBM studies.[11,34] Another MRI study reported no caudate atrophy in D-PD patients vs controls[35]; however, the measure used was whole caudate volume rather than gray matter density.

In a recent VBM study, D-PD patients were found to have a pattern of gray matter loss similar to dementia with Lewy bodies but different from Alzheimer disease (AD).[11] D-PD patients and patients with dementia with Lewy bodies both had widespread cortical (temporal, occipital, lateral prefrontal) and subcortical (caudate, putamen, thalamus) atrophy, with relative sparing of the medial temporal structures compared with control subjects and patients with AD. These results are at odds with those presented here. We found atrophy of the medial temporal lobe structures in the D-PD patients, consistent with previous reports in PD and similar to what has been

reported in AD.[27,36] A possible explanation is that our use of the DSM-IV criteria likely weighted our D-PD sample more toward memory impairment. Thus, the pattern of cerebral atrophy in D-PD most likely depends on the clinical characteristics of the patients studied.

There were no significant differences in medication dosages and clinical features, except MMSE scores, between the D-PD and ND-PD groups. However, the disease duration of D-PD tended to be longer than in ND-PD patients, consistent with a previous observation that longer disease duration is a risk factor for dementia in PD.[1,2] Thus, we cannot say whether atrophy of caudate and limbic/paralimbic and prefrontal areas is merely a result of disease progression or a feature specific to the subgroup of PD patients who develop dementia. Nonetheless, our results allow us to identify gray matter loss in these areas as the anatomic substrate of dementia in PD, a notion that is supported by the fact that co-varying out disease duration did not significantly affect the statistical map and also by the regression analysis in ND patients (see below). Finally, it should be noted that in our study, all D-PD patients had experienced visual hallucinations; therefore, our results may not generalize to PD patients with dementia and no hallucinations.

Regression analysis using RCPM score. Performance on the RCPM can be considered to involve both executive and visuospatial function in PD patients.[7] Previous PET activation studies with the Raven Progressive Matrices task (a variation of RCPM) in young healthy subjects showed a task-related increase of regional cerebral blood flow in areas involved in executive (prefrontal cortex) and visuospatial (occipital, parietal, and hippocampal/parahippocampal regions) function.[37] Therefore, our finding of a positive correlation between the RCPM score and gray matter density in the dorsolateral prefrontal cortex provides an explanation for executive dysfunction in PD. Although dopamine loss in the striatum may affect frontal lobe function by disrupting activity within basal ganglia–thalamocortical circuits,[38,39] our finding suggests that intrinsic frontal lobe degeneration may also play a role. We also observed a positive correlation between the RCPM score and gray matter density in the fusiform and parahippocampal gyri. This parahippocampal gyrus peak, which is more posterior than the parahippocampal gyrus peak in the D-PD vs ND-PD comparison, is in an area thought to be involved in the processing of spatial information.[40,41] Thus, atrophic change in the posterior part of the parahippocampal gyrus may lead to impairment of the visuospatial component of the RCPM.

PET activation with a delayed visual discrimination task that shares cognitive features with the RCPM has been reported.[42] In young subjects, the neutral network involved in this task was shown to include the prefrontal cortex (BA 10), fusiform gyrus, parahippocampal gyrus, posterior cingulate (precuneus), and inferior parietal gyrus. On the contrary, in the older subjects, the network included more anterior areas, namely, the caudate nucleus, dorsolateral prefrontal cortex (BA 9/46), and anterior cingulate gyrus (BA 32). Thus, in older subjects, the caudate nucleus is likely important in the RCPM task. However, in PD patients, because of the impairment of nigrostriatal dopaminergic projection, the network for the "young" (prefrontal cortex and fusiform/parahippocampal gyrus) may be recruited. Recruitment of the hippocampus during performance of a task that normally activates the caudate nucleus has previously been described in PD.[38] If such a recruitment is compensatory, damage to prefrontal and medial temporal structures would likely impair performance on the task. Indeed, we observed a significant correlation between the amounts of the gray matter and the RCPM performance in these two regions in our patients with PD.

RCPM performance did not correlate significantly with severity of PD motor symptoms in this current study, as also reported previously.[7] There is controversy regarding the effectiveness of dopamine replacement on cognitive impairment in PD.[43,44] In PD, the combined impairment of the basal ganglia–thalamocortical circuits due to dopamine deficiency and of the prefrontal cortex and parahippocampal gyrus due to gray matter atrophy may account for the lack of effect of dopamine repletion on cognition.

Acknowledgment

The authors thank Sylvain Milot (McConnell Brain Imaging Centre, Montreal Neurologic Institute, Montreal, Quebec, Canada) for technical help with images.

References

1. Giladi N, Treves TA, Paleacu D, et al. Risk factors for dementia, depression and psychosis in long-standing Parkinson's disease. J Neural Transm 2000;107:59–71.
2. Aarsland D, Tandberg E, Larsen JP, Cummings JL. Frequency of dementia in Parkinson disease. Arch Neurol 1996;53:538–542.
3. Dubois B, Pillon B. Cognitive deficits in Parkinson's disease. J Neurol 1997;244:2–8.
4. Janvin C, Aarsland D, Larsen JP, Hugdahl K. Neuropsychological profile of patients with Parkinson's disease without dementia. Dement Geriatr Cogn Disord 2003;15:126–131.
5. Raven JC. Standard Progressive Matrices: set A, A_B, B. London: Lewis, 1962.
6. Farina E, Gattellaro G, Pomati S, et al. Researching a differential impairment of frontal functions and explicit memory in early Parkinson's disease. Eur J Neurol 2000;7:259–267.
7. Cronin-Golomb A, Braun AE. Visuospatial dysfunction and problem solving in Parkinson's disease. Neuropsychology 1997;11:44–52.
8. Alegret M, Junque C, Pueyo R, et al. MRI atrophy parameters related to cognitive and motor impairment in Parkinson's disease. Neurologia 2001;16:63–69.
9. Hu MT, White SJ, Chaudhuri KR, Morris RG, Bydder GM, Brooks DJ. Correlating rates of cerebral atrophy in Parkinson's disease with measures of cognitive decline. J Neural Transm 2001;108:571–580.
10. Riekkinen P Jr, Kejonen K, Laakso MP, Soininen H, Partanen K, Riekkinen M. Hippocampal atrophy is related to impaired memory, but not frontal functions in non-demented Parkinson's disease patients. Neuroreport 1998;9:1507–1511.
11. Burton EJ, McKeith IG, Burn DJ, Williams ED, OBrien JT. Cerebral atrophy in Parkinson's disease with and without dementia: a comparison with Alzheimer's disease, dementia with Lewy bodies and controls. Brain 2004;127:791–800.
12. Calne DB, Snow BJ, Lee C. Criteria for diagnosing Parkinson's disease. Ann Neurol 1992;32(suppl):S125–S127.
13. McKeith IG, Galasko D, Kosaka K, et al. Consensus guidelines for the clinical and pathologic diagnosis of dementia with Lewy bodies (DLB):

report of the Consortium on DLB International Workshop. Neurology 1996;47:1113–1124.
14. Collins DL, Neelin P, Peters TM, Evans AC. Automatic 3D intersubject registration of MR volumetric data in standardized Talairach space. J Comput Assist Tomogr 1994;18:192–205.
15. Sled JG, Zijdenbos AP, Evans AC. A nonparametric method for automatic correction of intensity nonuniformity in MRI data. IEEE Trans Med Imag 1998;17:87–97.
16. Cocosco CA, Zijdenbos AP, Evans AC. A fully automatic and robust brain MRI tissue classification method. Med Image Anal 2003;7:513–527.
17. Smith S. Fast robust automated brain extraction. Hum Brain Map 2002;17:143–155.
18. Tohka J, Zijdenbos A, Evans AC. Fast and robust parameter estimation for statistical partial volume models in brain MRI. Neuroimage 2004; 23:84–97.
19. Poline JB, Worsley KJ, Evans AC, Friston KJ. Combining spatial extent and peak intensity to test for activations in functional imaging. Neuroimage 1997;5:83–96.
20. Schulz JB, Skalej M, Wedekind D, et al. Magnetic resonance imaging-based volumetry differentiates idiopathic Parkinson's syndrome from multiple system atrophy and progressive supranuclear palsy. Ann Neurol 1999;45:65–74.
21. Ghaemi M, Hilker R, Rudolf J, Sobesky J, Heiss WD. Differentiating multiple system atrophy from Parkinson's disease: contribution of striatal and midbrain MRI volumetry and multi-tracer PET imaging. J Neurol Neurosurg Psychiatry 2002;73:517–523.
22. Morecraft RJ, Geula C, Mesulam MM. Cytoarchitecture and neural afferents of orbitofrontal cortex in the brain of the monkey. J Comp Neurol 1992;323:341–358.
23. Braak H, Braak E. Pathoanatomy of Parkinson's disease. J Neurol 2000;247(suppl 2):3–10.
24. Harding AJ, Halliday GM. Cortical Lewy body pathology in the diagnosis of dementia. Acta Neuropathol (Berl) 2001;102:355–363.
25. Kövari E, Gold G, Herrmann FR, et al. Lewy body densities in the entorhinal and anterior cingulate cortex predict cognitive deficits in Parkinson's disease. Acta Neuropathol (Berl) 2003;106:83–88.
26. Churchyard A, Lees AJ. The relationship between dementia and direct involvement of the hippocampus and amygdala in Parkinson's disease. Neurology 1997;49:1570–1576.
27. Camicioli R, Moore MM, Kinney A, Corbridge E, Glassberg K, Kaye JA. Parkinson's disease is associated with hippocampal atrophy. Mov Disord 2003;18:784–790.
28. Mattila PM, Rinne JO, Helenius H, Dickson DW, Roytta M. Alpha-synuclein-immunoreactive cortical Lewy bodies are associated with cognitive impairment in Parkinson's disease. Acta Neuropathol (Berl) 2000;100:285–290.
29. Posner MI, Petersen SE, Fox PT, Raichle ME. Localization of cognitive operations in the human brain. Science 1988;240:1627–1631.
30. Duncan J, Owen AM. Common regions of the human frontal lobe recruited by diverse cognitive demands. Trends Neurosci 2000;23:475–483.
31. Taylor AE, Saint-Cyr JA, Lang AE. Frontal lobe dysfunction in Parkinson's disease. The cortical focus of neostriatal outflow. Brain 1986;109: 845–883.
32. Ito K, Nagano-Saito A, Kato T, et al. Striatal and extrastriatal dysfunction in Parkinson's disease with dementia: a 6-[18F]fluoro-L-dopa PET study. Brain 2002;125:1358–1365.
33. de la Monte SM, Wells SE, Hedley-Whyte T, Growdon JH. Neuropathological distinction between Parkinson's dementia and Parkinson's plus Alzheimer's disease. Ann Neurol 1989;26:309–320.
34. Brenneis C, Seppi K, Schocke MF, et al. Voxel-based morphometry detects cortical atrophy in the Parkinson variant of multiple system atrophy. Mov Disord 2003;18:1132–1138.
35. Almeida OP, Burton EJ, McKeith I, Gholkar A, Burn D, O'Brien JT. MRI study of caudate nucleus volume in Parkinson's disease with and without dementia with Lewy bodies and Alzheimer's disease. Dement Geriatr Cogn Disord 2003;16:57–63.
36. Laakso MP, Partanen K, Riekkinen P, et al. Hippocampal volumes in Alzheimer's disease, Parkinson's disease with and without dementia, and in vascular dementia: an MRI study. Neurology 1996;46:678–681.
37. Esposito G, Kirkby BS, Van Horn JD, Ellmore TM, Berman KF. Context-dependent, neural system-specific neurophysiological concomitants of ageing: mapping PET correlates during cognitive activation. Brain 1999;122:963–979.
38. Dagher A, Owen AM, Boecker H, Brooks DJ. The role of the striatum and hippocampus in planning: a PET activation study in Parkinson's disease. Brain 2001;124:1020–1032.
39. Lewis SJ, Dove A, Robbins TW, Barker RA, Owen AM. Cognitive impairments in early Parkinson's disease are accompanied by reductions in activity in frontostriatal neural circuitry. J Neurosci 2003;23:6351–6356.
40. Aguirre GK, Zarahn E, D'Esposito M. An area within human ventral cortex sensitive to "building" stimuli: evidence and implications. Neuron 1998;21:373–383.
41. Bar M, Aminoff E. Cortical analysis of visual context. Neuron 2003;38: 347–358.
42. Della-Maggiore V, Sekuler AB, Grady CL, Bennett PJ, Sekuler R, McIntosh AR. Corticolimbic interactions associated with performance on a short-term memory task are modified by age. J Neurosci 2000;20: 8410–8416.
43. Pillon B, Dubois B, Bonnet AM, et al. Cognitive slowing in Parkinson's disease fails to respond to levodopa treatment: the 15-objects test. Neurology 1989;39:762–768.
44. Costa A, Peppe A, Dell'Agnello G, et al. Dopaminergic modulation of visual-spatial working memory in Parkinson's disease. Dement Geriatr Cogn Disord 2003;15:55–66.